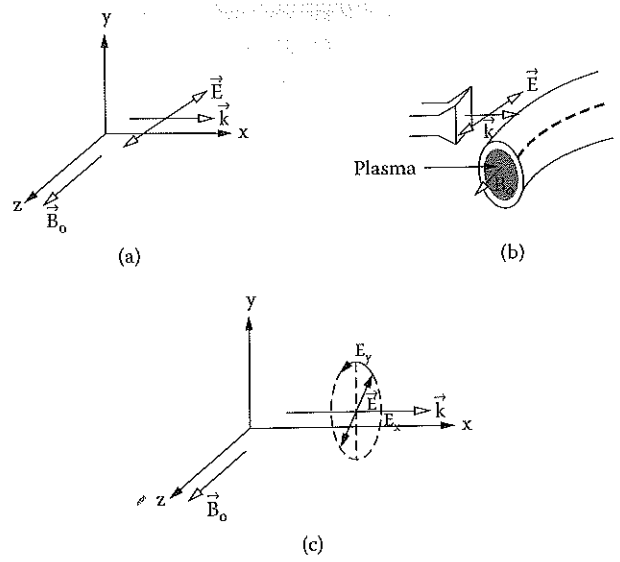

FIGURE 3.31
Models for propagation of modes in plasma: (a) O-mode, showing polarization of E; (b) geometry for O-mode plasma heating; (c) polarization for X-mode — note elliptical polarization of E.

- The *ordinary,* or O-, *mode,* with an electric field vector that is parallel to the magnetic field
- The *extraordinary,* or X-, *mode,* with electric field components in the x-y plane, i.e., perpendicular to the magnetic field, but with a component along the wavevector

In the case of the O-modes, because **E** and **k** are perpendicular to one another, $\nabla \cdot \mathbf{E} = 0$, so that there is no microwave space-charge associated with the wave. On the other hand, $\nabla \cdot \mathbf{E}$ does not vanish for the X-mode, so that there is a space-charge component to these waves. To describe the propagation of waves in the plasma, we turn to the concept of the dispersion relation, which is discussed in Chapter 4. Briefly, a dispersion relation is a mathematical relationship between $\omega = 2f$ and $k = 2/\lambda$ (λ is the wavelength along x), which for our purposes will be used to determine where waves may and may not propagate within the plasma and, consequently, where microwaves of a particular frequency and polarization should be launched. Here, we state the O- and X-mode dispersion relations without derivation (the interested reader is directed to Chen[59]):

- O-mode

$$k^2c^2 = \omega^2 - \omega^2_{pe} \tag{3.32}$$

where $\omega_{pe} = f_{pe}/2$

- X-mode

$$k^2c^2 = \frac{\left(\omega^2 - \omega_-^2\right)\left(\omega^2 - \omega_+^2\right)}{\omega^2 - \omega_{uh}^2} \tag{3.33}$$

with

$$\omega_\pm = \frac{1}{2}\left[\left(\omega_{ce}^2 + 4\omega_{pe}^2\right)^{1/2} \pm \omega_{ce}\right] \tag{3.34}$$

$$\omega_{uh}^2 = \omega_{ce}^2 + \omega_{pe}^2 \tag{3.35}$$

To demonstrate the relationship between the dispersion relations in Equations 3.32 and 3.33 and the ECRH frequency requirements, we consider first the O-mode waves with the dispersion relation given in Equation 3.32. There are some frequencies for which there are no real solutions for the wavenumber k; specifically, for frequencies below the plasma frequency, k is imaginary. The implication is that waves at those frequencies exponentially diminish in magnitude with distance into the plasma (causality rules out the growing wave solution in this case). Thus, waves with $\omega < \omega_{pe}$ cannot penetrate the plasma. In actual fusion plasma confined in the toroidal geometry of a tokamak, the plasma density increases from zero at the edges of the torus to a maximum somewhere near the center. On the other hand, the magnetic field, which is proportional to the cyclotron frequency ω_{ce}, is largest on the inner radius of the torus and decreases toward the outside radius. Applying our knowledge of wave dispersion to this inhomogeneous case, we construct the wave accessibility diagram shown in Figure 3.32a. There we have shaded those regions where locally the frequency is such that we cannot solve the dispersion relation for real values of k (i.e., where $\omega < \omega_{pe}$), on the assumption that waves will not penetrate those regions of the plasma. The electron cyclotron frequency will usually lie above the plasma frequency everywhere in such a plasma, so that waves with O-mode polarization should always be able to penetrate to the electron cyclotron resonance layer.

The X-mode situation is somewhat more complicated. Figure 3.32b shows the wave accessibility diagram for this polarization. We can see that waves are cut off for frequencies below ω_-, which is inconsequential because this frequency is less than ω_{ce} everywhere in the plasma. Additionally, however, no real solutions to the X-mode dispersion relation exist for values of ω between ω_{uh} and ω_+. Since one would not expect waves with frequencies in this cutoff range to pass through the cutoff layer, one cannot achieve electron cyclotron resonance for X-mode waves launched from the outside of the plasma; however, resonance at the electron cyclotron fundamental can be reached by launching these waves from the inner side of the torus. As a

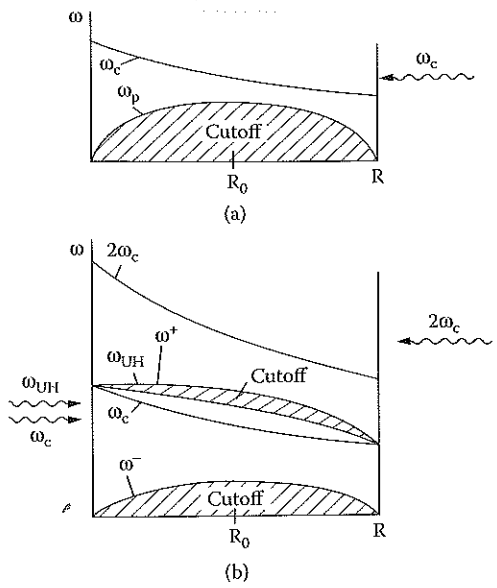

FIGURE 3.32
Wave accessibility diagrams for (a) O-mode and (b) X-mode propagation into plasma. R_0 is the plasma center and R is the edge. The torodial confining magnetic field decreases from inner to outer radius.

practical matter, this method of wave launching is usually undesirable because the inner surface of the torus is typically quite small and crowded. From this standpoint, it becomes desirable to generate X-mode waves at $2\omega_{ce}$, so that they can propagate to this resonant surface after launching from the outer surface of the plasma.

Other factors enter the process of selecting the optimal polarization and frequency for plasma heating. One of these is the strength of absorption at one of the resonant layers ($\omega = \omega_{ce}$ or $2\omega_{ce}$) for a wave with a given polarization. It turns out that the O-mode at $2\omega_{ce}$ is poorly absorbed at the early stages of plasma heating.[58] Therefore, the attractive choices are the O-mode at ω_{ce} and the X-mode at $2\omega_{ce}$, which have roughly equivalent absorption within the plasma. An additional practical consideration is that the production of a CW source at ω_{ce} (roughly 250 GHz at projected-fusion-reactor magnetic fields) with an average power of 1 MW is now a reality (Chapter 10), while the production of a 1-MW CW source at twice this frequency is somewhat more difficult. We therefore are left with O-mode waves at $\omega = \omega_{ce}$ as the primary immediate candidate for ECRH.

3.6.1 Sources for Electron Cyclotron Resonance Heating

Ten years ago, there were three candidate sources for ECRH. The survivor is the gyrotron, usually in a standard arrangement with the microwaves generated in a cavity aligned co-linearly with the beam (see Chapter 10). The other candidates were the cyclotron autoresonant maser (CARM), which promised high-frequency operation at high powers using more modest values of the guiding magnetic field, and the free-electron laser (FEL), which can operate continuously or in a repetitively pulsed, high-peak and average power mode. They were dropped on performance and cost grounds.

Although early heating experiments for fusion used gyroklystrons, and a free-electron laser was used in one experiment, all major ERCH experiments now employ gyro-oscillators. This is because the average power capabilities of gyro-oscillators make them far more desirable.

In addition, gyrotron oscillators have countered the extensive frequency tunability capabilities of gyro-amplifiers by using step tuning by varying the magnetic field in the gyrotron. High power, step-tunable gyrotrons are desirable for position-selective heating of fusion plasmas. Recent results have shown that ECRH can modify temperature profiles to suppress internal tearing modes. The frequency is adjusted to move the absorption region in the torus. This is achieved by using slow step tuning in which, as the magnetic field is varied over a broad range, the oscillation jumps from mode to mode, thus generating a broad and usually discrete radiation spectrum.

Gyrotron oscillators are now commercially available at average powers above 1 MW for times measured in seconds at frequencies of 75 to 170 GHz.[60] This is more than three orders of magnitude beyond the capability of other sources at these frequencies. The most ambitious experiment planned is the International Thermonuclear Experimental Reactor (ITER), which is to produce fusion power of 1 GW. With ECRH, a gyrotron pulse length of ~10^3 sec and power of ~100 MW will be required, meaning groups of gyrotrons operating simultaneously. Because cost is a driving factor, efficiencies greater than 50% will be necessary, and therefore depressed collectors will be essential. The present state of the art in the ITER frequency regime of 165 GHz is a coaxial gyrotron with 48% efficiency producing 2.2 MW.

3.7 Particle Accelerators

We test the limits of our knowledge of high-energy physics with the aid of high-energy accelerators. The triumphant standard model of particles and fields explains much, but is incomplete in not describing the necessary but elusive Higgs particle, as well as the particle masses themselves. The model also has no explanation for the dark matter that makes up 25% of the mass–energy of the universe, nor the dark energy, which is even larger. There are theories (e.g., supersymmetry, strings) of what lies at higher energies, but no accelerators are energetic enough to explore there. So, one line of accelerator development is aimed at the production of beams of electrons with energy of 1 TeV (1000 GeV). The accelerator producing such a beam

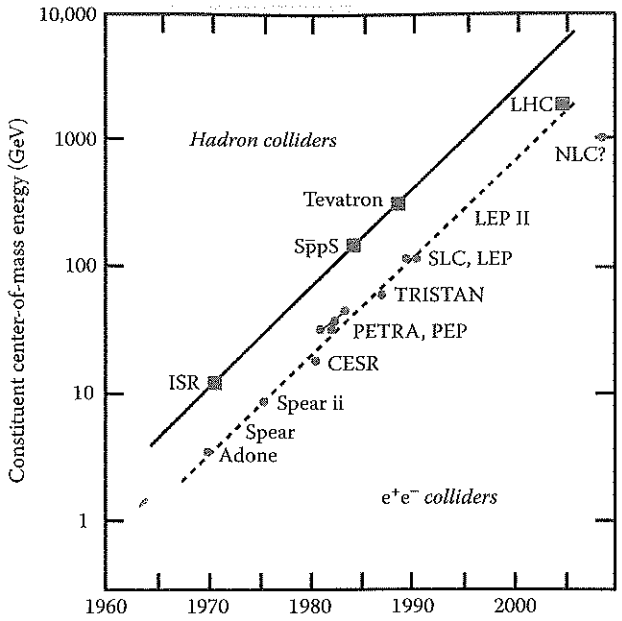

FIGURE 3.33
Evolution of accelerator beam energy for different accelerator types; circular accelerators of heavy particles on the left and linear electron accelerators (linacs) on the right.

will be an *RF accelerator*, in which radio frequency sources (actually microwave, as all approaches operate above the 0.3-GHz boundary between radio and microwave frequencies) produce the electric fields that accelerate the electrons. The evolution of particle accelerators in general, both electron and hadron (heavy particles such as protons) accelerators, is shown in Figure 3.33. Ion accelerators for protons and heavier nuclei use low frequencies (<1 GHz) for acceleration, basically because they are slow compared to the much lighter electrons. The state-of-the-art electron accelerators are the Stanford Linear Collider (SLC; 2.5 GHz, 45 GeV) at the Stanford Linear Accelerator Center (SLAC) in Palo Alto, CA, and the Large Electron-Positron (LEP; 209 GeV) Collider at the European Center for Nuclear Research (CERN) near Geneva, Switzerland. Both produce beams of high-energy electrons and positrons that collide and annihilate each other, generating as a result subatomic particles that provide information about the basic nature of matter and the elementary forces. The SLC, completed in 1987 and soon to be closed, has a linear accelerator, or *linac*, 3 km in length, producing 45-GeV particles. LEP is a large ring-shaped accelerator with a circumference of 26.7 km, initially producing oppositely directed beams of 55-GeV electrons and positrons, now with collision energy to 209 GeV.[61]

Because the synchrotron radiation losses of centrifugally accelerated electrons scale as E^4/R^2, with E the electron energy and R the radius of curvature of the electron orbit,[62] a 1-TeV electron accelerator will be linear. The power needed to drive electrons to such energies is far greater than a single source can supply, so gangs of sources are made to operate in phase synchronism. Amplifiers are used, though phase-locked oscillators can in principle work as well, especially for the smaller energies needed for industrial uses such as radiography and cancer therapy.

A key performance parameter for RF linacs is the accelerating gradient, the rate at which the energy of the electrons increases, measured in MeV/m. The higher the gradient, the shorter a linac can be made for a given final energy. This translates to lower costs for an accelerator, in terms of both hardware and site acquisition costs. The average SLC gradient is 17 MeV/m (the gradient within the accelerating sections is somewhat higher). The goal for a TeV machine is an accelerating gradient of the order of 100 MeV/m or more. As we will discuss shortly, meeting this goal is not possible at present and will require serious improvement in accelerator technology. Gradient increases with frequency because breakdown strengths also increase with frequency. On the other hand, the resonant cavities along the accelerator also become smaller with increased frequency, which reduces margins and tolerances, so much effort has been dedicated to accelerating efficiently through the smaller structures.

Achievement of higher-accelerating gradients would have the added benefit of making lower-energy RF linacs used in medical and industrial applications more compact. We mention two of these applications to illustrate their importance. If electrons are allowed to strike a metallic bremsstrahlung converter, in which their kinetic energy is converted to x-rays, they can be used for industrial radiography or cancer therapy. The energetic electron beams can also be passed through magnetic *undulators* or *wigglers* to produce synchrotron light sources or free-electron lasers (described in Chapter 10).

Much advanced HPM source research has been motivated by the need for higher-energy accelerators. Before we discuss the role HPM sources will play in meeting the goals of higher energy and very high accelerating gradient, we briefly review the basic principles of linacs. Figure 3.34 contains a block diagram for an RF linac. Within the accelerating sections, bunches of electrons are accelerated by the axial electric field component of HPM, as shown in Figure 3.35. The microwaves are produced in pulses of finite duration known as the *macropulse*, while an individual electron bunch is known as a *micropulse*. The number of RF wavelengths between micropulses is known as the *subharmonic number*. The bunched beam for the accelerator is produced in an injector. Of the two main types of injectors, the more common is the lower one shown in the figure, in which electrons from a source are initially accelerated into a bunching section. The bunching section is much like an accelerating section, except that in the *buncher*, electrons that may initially be uniformly distributed along the axis are either accelerated or decelerated according to the phase of the RF signal that they experience. This process, known as *autophasing*, will bunch the electrons in the potential wells of the RF. A second type of injector under development, known as a *photoinjector*, works by pulsed-laser illumination of a cathode made of a

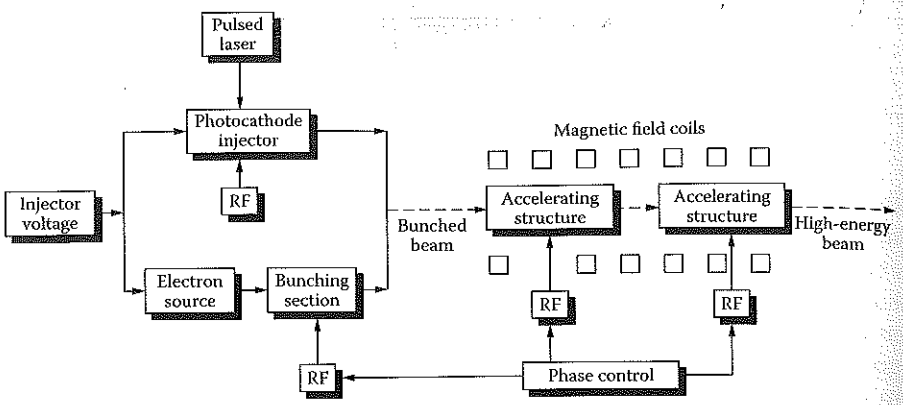

FIGURE 3.34
Diagram of microwave-driven electron linear accelerator. Photocathode injector or conventional electron source produces bunched beam that is injected into the accelerating cavities.

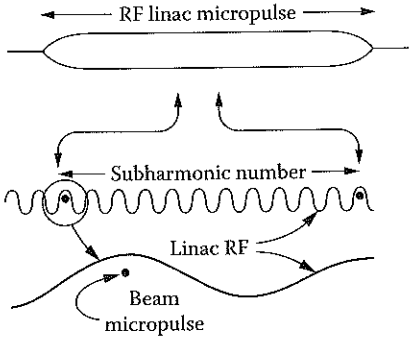

FIGURE 3.35
Electron beam micropulses within the macropulse in an RF wave of a microwave-driven linac.

photoemitting material. With the laser pulsed at the proper frequency, bunches with the proper spacing for the accelerating section can be made in this way.

The accelerating sections tailor properties of the microwave fields so that they can effectively interact with the electron bunches. An example of an accelerating section is shown in Figure 3.36. These sections work in one of two basic fashions. In the *traveling wave accelerator*, the RF is fed into the section at one end and travels through the section with its phase in synchronism with the bunches so that they feel a constant accelerating force; at the exit end of the section, the RF is absorbed. In a *standing wave accelerator*, the RF fields are arranged in a standing wave pattern, with zero-phase velocity along the section axis; the frequency and phase of the fields will be such that the bunch always feels an accelerating polarity of the fields as it passes from cavity to cavity in the accelerating section.

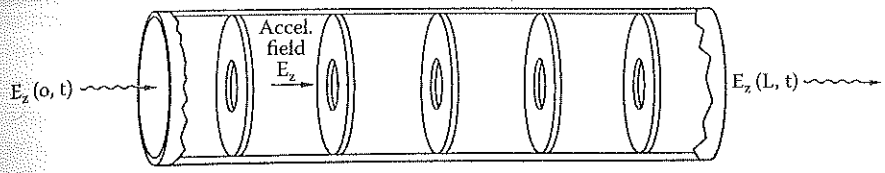

FIGURE 3.36
Accelerating section of a microwave-driven linac using disk-loaded waveguide of length L.

For decades, three accelerating technologies have been under development: copper RF cavities, superconducting RF cavities, and two-beam (also called driving-beam) acceleration. The copper cavity (warm) approach is an evolution of SLC and uses higher-frequency high power (~100-MW) relativistic klystrons, as described in Chapter 9. At SLC this method achieved a 50-MV/m gradient. The superconducting cavities (cold) approach offers higher efficiency, but lower accelerating gradient (~30 MV/m vs. ~100 MV/m projected for copper in future development).

A number of more speculative options are being explored to reach TeV energy levels with accelerating gradients of the order of 100 MeV/m. Some of these are quite speculative and lie outside the scope of our discussion: *wake field* accelerators, switched power accelerators, and laser *beat wave* and wake field accelerators using a plasma medium.[63]

Less speculative, but still unproven on a large scale, is the *two-beam accelerator*.[64] An electron beam at low energy and high current is used to produce HPM, which then accelerate electron bunches in an RF accelerator to high energies. The idea is not unlike that of a transformer from low voltage and high current to high voltage and low current. A possible configuration for such an accelerator using a free-electron laser to generate the RF is shown in Figure 3.37. An intense electron beam with an energy and current of the order of several MeV and several kA is generated in an induction linac, and microwaves are produced in the FEL wiggler sections and transmitted to the high-energy RF linac through the microwave power feeds; the energy tapped from the drive beam in the FEL is replenished in additional induction sections.

The decision has been made to build the International Linear Collider with the cold option, superconducting RF cavities. The decision was on cost/risk grounds and the fact that Germany is already building a coherent light source using the cold technology.[65] The sources required for the cold method are not nigh power, in contrast to the ~100-MW klystrons of the hot method. The candidates are ~10-MW, 1-msec multibeam klystrons.

The two-beam approach is being carried forward for multi-TeV energies by CERN, in a version different from that of Figure 3.37 called CLIC (Compact Linear Collider),[66] aiming for 3 to 5 TeV. The method is complex, with the ultimate acceleration driven by 30-GHz pulses at powers of several hundred MW. In the present concept, the CLIC Power Extraction and Transfer Structure (PETS) is a passive microwave device where bunches of the

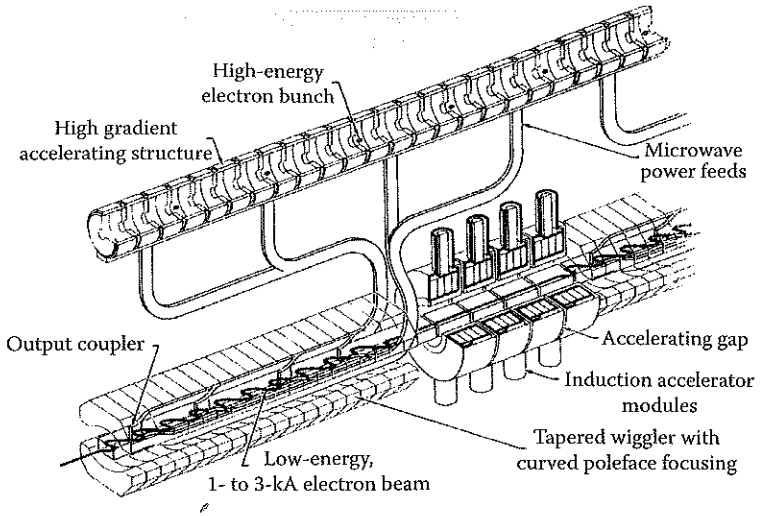

FIGURE 3.37
Two-beam accelerator concept. This type uses a free-electron laser, driven by an electron beam of several kA — several MeV to produce microwaves for the high-gradient accelerating structure of a linac. Induction modules (see Chapter 5) resupply the beam energy lost to microwaves.

drive beam interact with the impedance of a periodically corrugated waveguide and preferentially excite the synchronous traveling wave TM01 mode at 30 GHz.[67] The microwave power produced is collected at the downstream end of the structure by means of the power extractor and is conveyed to the main linac structure in rectangular waveguides. Principal issues are high surface electric and magnetic fields and simply how to build such a complex and carefully aligned system.

CLIC needs high power (~50-MW), long-pulse (~100-sec), 937-MHz multibeam klystrons (see Chapter 9) to supply the RF power needed to accelerate the low-energy, high-intensity drive beam. The CLIC technology is not yet mature; challenging R&D is required.

The 30-GHz CLIC two-beam is the only method that promises to reach the >100-MV/m regime, making >1-TeV electron colliders possible. The sub-TeV energy range will be explored initially by the Large Hydron Collider (LHC) by 2010. If that range is not found to give physics results attractive enough to build ILC with cold technology, and if particle physicists feel multi-TeV energies are needed to access physics interesting enough to justify the cost of such a large project, CLIC is the alternative to the ILC.

A limiting factor in accelerating gradient is the electric field breakdown limit in the accelerating structure. Breakdown in normal conducting traveling wave structures has been observed to variously depend on a number of parameters, including surface electric field, pulse length, power flow, and group velocity. Current research gives a limit that is determined over the frequency range of 3 to 30 GHz by the quantity $P\tau^{1/3}/C$, where P is the microwave power flow through the structure, τ is the pulse length, and C is the minimum circumference of the structure. This result comes from experiment.[68] The physical interpretation is that division of power by circumference gives the power flow above a unit transverse width of structure surface. This linear power density is the local power available to feed a discharge, which determines local heating of the structure surface. A limit is reached when the heating causes ablation of the surface material. When the temperature rise due to heat diffusion is caused solely by a constant deposited power, the ablation limit has a square-root time dependence. When an additional cooling mechanism, such as boiling, evaporation, radiation, or two-dimensional heat conduction, is included though, the time dependence of the limit is weaker and $\tau^{1/3}$ becomes plausible.

Breakdown strength also scales up with frequency, going approximately as $f^{7/8}$, experiments show. So higher frequencies can be more attractive, which is one reason CLIC chooses to operate at 30 GHz. As the frequency increases, certain other desirable features are seen: energy stored in the accelerating section and the average RF power required decrease as f^{-2}, dissipation within the structure and the peak RF power required decrease as $f^{-1/2}$, and the section length diminishes as $f^{-3/2}$.

Not all scalings are favorable, however. The dimensions of the accelerating structures scale as the wavelength of the microwaves ~f^{-1}. This means that the size of a structure designed for operation at 30 GHz is measured in millimeters. Hence, tolerances on structure fabrication and beam location become more difficult to meet. Beam quality problems are also exacerbated at higher frequencies by the *wake fields* that are excited by the passage of the electron bunch through the accelerating structure. Roughly speaking, the bunch acts as an impulse that can excite higher-order, undesired modes of the structure. The wake fields associated with these modes can be longitudinal or transverse. The longitudinal wake fields increase as f^2 and cause longitudinal energy spread and a resultant bunch elongation. The transverse wake fields increase as f^3 and tend to push the beam off axis. Overall, at the currents needed in linear colliders, the reduced structure dimensions and increased wake field magnitudes accompanying the higher RF frequencies limit the upper accelerating frequency to about 30 GHz at present.

Problems

1. An HPM technologist, reporting on a device he has built, claims the efficiency of producing microwaves is 56%. The device produces 3 GW in a 100-nsec microwave pulse. The electrical input from a Marx/pulse-forming network (PFN) (see Section 5.2) is at 5.35 GW. This looks good to you for your application. However, you notice that the weight of the contractor's pulsed power system is half a ton

(about 500 kg), much too heavy for your platform. You know that Marx/PFNs typically are available at 300 g/J. What is the contractor not telling you?

2. To scope the effect that Active Denial relies on, suppose a 94-GHz signal is incident on salt water with conductivity at a frequency of 4.3 S/m. What is the skin depth (skin depth of a lossy dielectric material is given by Equation 4.51)? If the conductivity for human skin is 17 S/m, compute the skin depth.
3. If the Vigilant Eagle system attacks a missile with a lethality threshold of 1 mW/cm^2, at a range of 5 km from the airfield to the missile and a beam width of 1°, what transmitter power is required?
4. A missile target is measured to have a power coupled to circuitry inside of 1 W with 100 W/cm^2 incident power. Your tests show that 1 W coupled inside will produce mission failure. To get high P_k you must operate in X-band. Your mission analysis shows that for ensured kill you must defeat the missile at a range of at least 5 km. Your platform allows an antenna aperture no greater than 1 m, and you estimate the antenna efficiency as 60%. What is the coupling cross section? What is the minimum power radiated from the antenna required for this mission? What is the beam size at the target?
5. For NAGIRA, the BWO is reported to have an output of 0.5 GW. What is the microwave production efficiency of the BWO? If frequency stability requires that pulse-to-pulse microwave power be regulated to within 1%, and efficiency of microwave generation is independent of voltage, and the BWO diode is described by Child's law, what pulse-to-pulse voltage variation is allowed?
6. There is an optimum range of power density to operate a rectenna, set by the rectification efficiency of diodes (Figure 3.20). You want to change the operating frequency on a rectenna, but keep both the power beaming antenna aperture and the range to the rectenna fixed. You will need a new rectenna, and to keep efficiency up, will keep its area just large enough to fill the half-power beam width. You know that the area served by a single dipole in the rectenna (Figure 2.19) is proportional to the square of the wavelength. How does the number of dipole/diode elements you need vary with frequency? How does the power per diode vary?
7. Using the rocket equation, for mass ratios of 10, 100, and 1000, what multiples of exhaust velocity can a rocket achieve?
8. What force occurs on a 100-kg perfectly reflecting sail for 1-GW incident beam power? How long would the beam have to accelerate the sail to reach an interplanetary-scale speed of 1 km/sec?
9. For a beam-driven sail, at what range does the beam width size exceed the sail size? If power is constant in time, what speed is attained at this point? How much more speed results if the beam remains on beyond this point?
10. In a sail using desorption-driven propulsion we measure the temperature T*, at the peak in the desorption rate dn/dt, as 2000 K. At this time, dn/dt is given by Equation 3.15 and $dT^*/dt = bT^*$. If b/a = 0.5, what value of Q did the desorbing material have?
11. Model the capital cost C_C of an interstellar beamer as the cost of aperture with an areal cost coefficient of $B_1(\$/m^2)$, plus the cost of power with coefficient $B_2(\$/W)$. Find the value of beamer diameter D_t and power P that minimizes the cost for accelerating a mass m to a fraction k of the speed of light. Take r as the ratio of beamer diameter D_t to the diameter of the sail riding the beam, d. First, note that at maximum useful beaming range R, the sail diameter d is approximately the diffraction-limited beam width. Find an expression for the maximum useful accelerating time. Find P in terms of D and use Dickinson's observation that minimum cost for this two-parameter model occurs when the cost of power is equal to the cost of aperture. For a light 100-kg sail probe and r = 275, what diameter beamer and power are optimum at 100 GHz?

References

1. Rawles, J., Directed energy weapons: battlefield beams, *Defense Electronics*, 22, 47, 1989.
2. Taylor, T., Third generation nuclear weapons, *Sci. Am.*, 256, 4, 1986.
3. Price, D. et al., Compact pulsed power for directed energy weapons, *J. Directed Energy*, 1, 48, 2003.
4. Benford, J. and Benford, G., Survey of pulse shortening in high power microwave sources, *IEEE Trans. Plas. Sci.*, 25, 311, 1997.
5. Kopp, C., Electromagnetic Bomb, a Weapon of Electromagnetic Mass Destruction, http://abovetopsecret.com/pages/ebomb.html, 2003.
6. Beason, D., *The E-Bomb*, Da Capo Press, Cambridge, MA, 2005.
7. Introduction to FLAPS, http://www.maliburesearch.com/advancedAnt21_IntroFlaps.html.
8. Fulghum, D., Microwave weapons emerge, in *Aviation Week & Space Technology*, www.AviationNow.com/awst, 2005.
9. Singer, J., USAF interest in lasers triggers concerns about anti-satellite weapons, *Space News*, 17, A4, 2006.
10. Velikhov, V., Sagdeev, R., and Kokashin, A., *Weaponry in Space: The Dilemma of Security*, MIR Press, Moscow, 1986.
11. Wunsch, D.C. and Bell, R.R., Determination of threshold failure levels of semiconductor diodes and transistors due to pulsed power voltages, *IEEE Trans. Nucl. Sci.*, NS-15, 244, 1968.
12. Hoad, R. et al., Trends in susceptibility of IT equipment, *IEEE Trans. Electromag. Compatibility*, 46, 390, 2004.

13. Mannheimer, W., Applications of high-power microwave sources to enhanced radar systems, in *Applications of High Power Microwaves*, Gaponov-Grekov, A.V. and Granatstein, V., Eds., Artech House, Boston, 1994, chap. 5, p. 169.
14. Clunie, D. et al., The design, construction and testing of an experimental high power, short-pulse radar, strong microwave, in *Plasmas*, Litvak, A.G., Ed., Novgorod University Press, Nizhny Novgorod, Russia, 1997.
15. Baum, C. et al., The singularity expansion method and its application to target identification, *Proc. IEEE*, 79, 1481, 1991.
16. Nalos, E., New developments in electromagnetic energy beaming, *Proc. IEEE*, 55, 276, 1978.
17. McSpadden, J. and Chang, K., *Microwave Power Transmission*, Wiley Inter-Science, New York, in press.
18. Benford, J., Modification and measurement of the atmosphere by high power microwaves, in *Applications of High Power Microwaves*, Gaponov-Grekov, A.V. and Granatstein, V., Eds., Artech House, Boston, 1994, chap. 12, p. 209.
19. Pozar, D.M., *Microwave Engineering*, 2nd ed., John Wiley & Sons, New York, 1998, p. 665.
20. Hansen, R.C., McSpadden, J., and Benford, J., A universal power transfer curve, *IEEE Microwave Wireless Components Lett.*, 15, 369, 2005.
21. Koert, P. and Cha, J., Millimeter wave technology for space power beaming, *IEEE Trans. Microwave Theory Tech.*, 40, 1251, 1992.
22. Dickinson, R.M., Wireless power transmission technology state-of-the-art, in *Proceedings of the 53rd International Astronautical Congress*, Houston, 2002.
23. McSpadden, J. and Mankins, J., Space solar power programs and wireless power transmission technology, *IEEE Microwave Mag.*, 3, 46, 2002.
24. Dickinson, R.M., Performance of a high-power, 2.388 GHz receiving array in wireless power transmission over 1.54 km, in *1976 IEEE MTT-S International Microwave Symposium*, Cherry Hill, NJ, 1976, p. 139.
25. Brown, W.C., Beamed microwave power transmission and its application to space, *IEEE Trans. Microwave Theory Tech.*, 40, 123, 1992.
26. National Research Council, *Laying the Foundation for Space Solar Power: An Assessment of NASA's Space Solar Power Investment Strategy*, National Academy Press, Washington, DC, 2001.
27. Glaser, P., Davidso, F., and Csigi, K., *Space Solar Satellites*, Praxis Publishing, Chichester, U.K., 1998.
28. Fetter, S., Space solar power: an idea whose time will never come? *Physics and Society*, 33, 10, 2004. See also reply in Smith, A., Earth vs. space for solar energy, round two, *Physics Soc.*, 33, ?, 2002.
29. Criswell, D.R., Energy prosperity within the 21st century and beyond: options and the unique roles of the sun and the moon, in *Innovative Solutions to CO_2 Stabilization*, Watts, R., Ed., Cambridge University Press, Cambridge, U.K., 2002, p. 345.
30. Hoffert, M., Miller, G., Kadiramangalam, M., and Ziegler, W., Earth-to-satellite microwave power transmission, *J. Propulsion Power*, 5, 750, 1989.
31. Matloff, G., *Deep-Space Probes*, 2nd ed., Springer-Verlag, New York, 2005.
32. Zaehringer, A.J., *Rocket Science*, Apogee Books, Burlington, Ontario, 2004.
33. Parkin, K.L.G., DiDomenico, L.D., and Culick, F.E.C., The microwave thermal thruster concept, in *AIP Conference Proceedings 702: Second International Symposium on Beamed-Energy Propulsion*, Komurasaki, K., Ed., Melville, NY, 2004, p. 418.
34. Parkin, K.L.G. and Culick, F.E.C., Feasibility and performance of the microwave thermal rocket launcher, in *AIP Conference Proceedings 702: Second International Symposium on Beamed-Energy Propulsion*, Komurasaki, K., Ed., Melville, NY, 2004, p. 407.
35. Parkin, K.L.G., DiDomenico, L.D., and Culick, F.E.C., The microwave thermal thruster concept, in *AIP Conference Proceedings 702: Second International Symposium on Beamed-Energy Propulsion*, Komurasaki, K., Ed., Melville, NY, 2004, p. 418.
36. Parkin, K.L.G. and Culick, F.E.C., Feasibility and performance of the microwave thermal rocket launcher, in *AIP Conference Proceedings 664: Second International Symposium on Beamed-Energy Propulsion*, Komurasaki, K., Ed., Melville, NY, 2003, p. 418.
37. Benford, J. and Myrabo, L., Propulsion of small launch vehicles using high power millimeter waves, *Proc. SPIE*, 2154, 198, 1994.
38. Benford, J. and Dickinson, R., Space propulsion and power beaming using millimeter systems, *Proc. SPIE*, 2557, 179, 1995. Also published in *Space Energy Transp.*, 1, 211, 1996.
39. Hoppe, D.J. et al., Phase locking of a second harmonic gyrotron using a quasi-optical circulator, *IEEE Trans. Plas. Sci.*, 23, 822, 1995.
40. Lineberry, J. et al., MHD augmentation of rocket engines using beamed energy, in *AIP Conference Proceedings 608: Space Technology and Applications International Forum*, Huntsville, AL, 2003, p. 280.
41. Benford, G. and Benford, J., An aero-spacecraft for the far upper atmosphere supported by microwaves, *Acta Astronautica*, 56, 529, 2005.
42. Kare, J.T. and Parkin, K.L.G., Comparison of laser and microwave approaches to CW beamed energy launch, beamed energy propulsion — 2005, in *AIP Conference Proceedings 830: American Institute of Physics*, Komurasaki, K., Ed., Melville, NY, 2006, p. 388.
43. McInnes, C., *Solar Sailing: Technology, Dynamics, and Mission Applications*, Springer-Verlag, New York, 1999.
44. Forward, R.L., Starwisp: an ultra-light interstellar probe, *J. Spacecraft*, 22, 345, 1985.
45. Landis, G.A., Microwave-Pushed Interstellar Sail: Starwisp Revisited, paper AIAA-2000-3337, presented at the 36th Joint Propulsion Conference, Huntsville, AL, 2000.
46. Benford, J. and Benford, G., Flight of microwave-driven sails: experiments and applications, in *AIP Conference Proceedings 664: Beamed Energy Propulsion*, Pakhomov, A., Ed., Huntsville, AL, 2003, p. 303.
47. Cuneo, M.E., The effect of electrode contamination, cleaning and conditioning on high-energy pulsed-power device performance, *IEEE Trans. Dielectrics Electrical Insulation*, 6, 469, 1999. See also Cuneo, M.E. et al., Results of vacuum cleaning techniques on the performance of LiF field-threshold ion sources on extraction applied-B ion diodes at 1–10 TW, *IEEE Trans. Plas. Sci.*, 25, 229, 1997.
48. Benford, G. and Nissenson, P., Reducing solar sail escape times from earth orbit using beamed energy, *JBIS*, 59, 108, 2006.
49. Landis, G., Beamed energy propulsion for practical interstellar flight, *JBIS*, 52, 420, 1999.
50. Benford, G. and Benford, J., Power-beaming concepts for future deep space exploration, *JBIS*, 59, 104, 2006.
51. Schamiloglu, E. et al., 3-D simulations of rigid microwave propelled sails including spin, *Proc. Space Technol. Appl. Int. Forum AIP Conf. Proc.*, 552, 559, 2001.

52. Benford, G., Goronostavea, O., and Benford, J., Experimental tests of beam-riding sail dynamics, in *AIP Conference Proceedings 664: Beamed Energy Propulsion*, Pakhomov, A., Ed., Huntsville, AL, 2003, p. 325.
53. Benford, G. and Benford, J., An aero-spacecraft for the far upper atmosphere supported by microwaves, *Acta Astronautica*, 56, 529, 2005.
54. Konz, C. and Benford, G., Geometric absorption of electromagnetic angular momentum, *Optics Commun.*, 226, 249, 2003.
55. Benford, G., Goronostavea, O., and Benford, J., Spin of microwave propelled sails, in *AIP Conference Proceedings 664: Beamed Energy Propulsion*, Pakhomov, A., Ed., Huntsville, AL, 2003, p. 313.
56. Benford, J. and Benford, G., Elastic, electrostatic and spin deployment of ultralight sails, *JBIS*, 59, 76, 2006.
57. Prather, R., Heating and current drive by electron cyclotron waves, *Phys. Plas.*, 11, 2349, 2004.
58. Ott, E., Hui, B., and Chu, K.R., Theory of electron cyclotron resonance heating of plasmas, *Phys. Fluids*, 23, 1031, 1980.
59. Chen, F., *Introduction to Plasma Physics*, Plenum Press, New York, 1974, chap. 4.
60. Felch, K.L. et al., Characteristics and applications of fast-wave gyrodevices, *Proc. IEEE*, 87, 752, 1999.
61. Hinchliffe, I. and Battaglia, M., A TeV linear collider, *Physics Today*, 57, 49, 2004.
62. Humphries, S., *Principles of Charged Particle Acceleration*, John Wiley & Sons, New York, 1986.
63. Chandrashekhar, J., Plasma accelerators, *Sci. Am.*, 294, 40, 2006.
64. Sessler, A. and Yu, S., Relativistic klystron two-beam accelerator, *Phys. Rev. Lett.*, 58, 243, 1987.
65. Gamp, G., On the preference of cold RF technology for the International Linear Collider, in *AIP Conference Proceedings 807: High Energy Density and High Power RF, 7th Workshop*, Kalamata, Greece, 2006, p. 1.
66. Van Der Mear, S., The CLIC approach to linear colliders, *Part. Accel.*, 30, 127, 1990.
67. Battaglia, M. et al., Ed., Physics at the CLIC Multi-TeV Linear Collider, report CERN 2004-005 of the CLIC Physics Working Group, http://documents.cern.ch/cernrep/2004/2004-005/2004005.html.
68. Wuensch, W., The Scaling Limits of the Traveling-Wave RF Breakdown Limit, report CERN-AB-2006-013, CLIC Note 649, 2006.

4

Microwave Fundamentals

4.1 Introduction

High power microwaves are generated by transferring the kinetic energy of moving electrons to the electromagnetic energy of the microwave fields.* This process typically occurs in a waveguide or cavity, the role of which is to tailor the frequency and spatial structure of the fields in a way that optimizes the energy extraction from certain natural modes of oscillation of the electrons. In analyzing this process, we deal with the interactions between two conceptual entities: the normal electromagnetic modes of the waveguides and cavities and the natural modes of oscillation of electron beams and layers. The two exist almost independently of one another except for certain values of the frequency and wavelength, for which they exchange energy resonantly. We will therefore begin the chapter by reviewing the basic concepts of electromagnetics and considering the fields within waveguides in the absence of electrons. Our emphasis will be on two key properties of the electromagnetic fields within the waveguide: the spatial configuration of the fields and the relationship between the oscillation frequency and wavelength measured along the system axis. Our treatment will include both smooth-walled waveguides and periodic slow-wave structures, the treatment of the latter requiring a discussion of Floquet's theorem and Rayleigh's hypothesis. We will also touch on two features that play a role in determining the power-handling capability of high power devices: the relationship between the power in a waveguide or cavity and the peak perpendicular field at the wall, a key factor in breakdown, and resistive wall heating in high-average-power devices, either continuous or rapidly pulsed. From waveguides, we will graduate to cavities, which have normal modes of their own that can be treated largely by extension from the treatment of waveguides. The important cavity parameter Q, the so-called *quality factor*, will be a focus of the discussion.

* An exception to this is Hertzian oscillators, or wideband and ultrawideband sources such as those described in Chapter 6, in which microwaves are generated by direct coupling between a pulsed power source and an antenna.

Having introduced the key electromagnetic field concepts, we next consider space-charge-limited flow of electrons, both in a diode and for a beam in a drift tube, concepts that are key to the discussion of virtual cathodes. We follow this with a brief discussion of beam propagation, beam equilibria, and the formation of electron layers. We then proceed to a discussion of the natural modes of oscillation on electron beams and layers, and classify the different microwave sources according to the nature of the electron oscillations that facilitate the transfer of electron energy to the fields. Following that, we will take two alternative views of source classification, first by differentiating between oscillators and amplifiers, and then by considering the high- and low-current regimes of operation. We then proceed to address the topic of phase control between multiple sources being made to act in concert. Finally, we conclude with a discussion of the disposition of the spent electron beam downstream of the electromagnetic interaction region.

4.2 Basic Concepts in Electromagnetics

The electric and magnetic fields **E** and **B** in a microwave device are driven by the charge and current densities ρ and **j** according to Maxwell's equations, which are the following:

$$\nabla \times \mathbf{B} = \mu_0 \mathbf{j} + \frac{1}{c^2}\frac{\partial \mathbf{E}}{\partial t} \tag{4.1}$$

$$\nabla \times \mathbf{E} = -\frac{\partial \mathbf{B}}{\partial t} \tag{4.2}$$

$$\nabla \bullet \mathbf{B} = 0 \tag{4.3}$$

$$\nabla \bullet \mathbf{E} = \frac{\rho}{\varepsilon_0} \tag{4.4}$$

On occasion, some use the alternate field variables $\mathbf{D} = \varepsilon\mathbf{E}$ and $\mathbf{H} = \mathbf{B}/\mu$, where ε and μ are generalized values of the permittivity and permeability, equal to ε_0 and μ_0 in a vacuum. The solutions to these equations must conform to certain boundary conditions, which play an important role in determining the mode parameters in a waveguide or cavity, particularly when the mode wavelengths are comparable to the geometrical dimensions of the waveguide or cavity involved. The most straightforward boundary conditions are those that apply at the surface of a perfect conductor. At the surface of a perfect conductor, the tangential component of the electric field and the perpendicular component of the magnetic field must vanish. Therefore, at a point **x** on the surface of the conductor, with $\mathbf{n}_t$ a unit vector* tangential to the surface and $\mathbf{n}_p$ a unit vector perpendicular to the surface,

$$\mathbf{n}_t \bullet \mathbf{E}(\mathbf{x}) = 0 \tag{4.5}$$

$$\mathbf{n}_p \bullet \mathbf{B}(\mathbf{x}) = 0 \tag{4.6}$$

The perpendicular component of **E** and the tangential component of **B**, however, can be discontinuous at the surface by an amount equal to the surface charge density and surface current density at the surface; these can be determined by integrating Equations 4.1 and 4.4 across the surface, which we shall discuss in context later in the chapter. We will also defer a discussion of the effect of a finite electrical conductivity σ at the surface.

The source terms ρ and **j** arise as a consequence of motion by individual electrons in response to the fields according to Newton's law,

$$\frac{d\mathbf{p}}{dt} = -e(\mathbf{E} + \mathbf{v} \times \mathbf{B}) \tag{4.7}$$

in which the momentum $\mathbf{p} = m\gamma\mathbf{v}$, where m is the mass of an electron, **v** is the velocity of an electron, and the relativistic factor $\gamma = (1 - |\mathbf{v}|^2/c^2)^{-1/2}$. Calculation of ρ and **j** involves some sort of summing process on the electrons. This closure process of relating electron motions back to the source terms in Maxwell's equations is an important element of any theoretical treatment. A wide variety of techniques are available for this task. For example, if the electrons in a beam or layer can be treated as a fluid, the momentum and velocity in Equation 4.7 can be treated as the momentum and velocity of a fluid element obeying the same equation, and the current density can be written

$$\mathbf{j} = \rho\mathbf{v} \tag{4.8}$$

Alternatively, if there is a considerable variation of the electron velocities about some mean — as would be the case for a beam with substantial divergence or axial velocity spread — then a classical approach based on the Vlasov or Boltzmann equations might be more appropriate. With the wide availability of computers, numerical techniques are increasingly applied. In any event, those who deal with theoretical treatments of microwave systems must be careful to evaluate the validity of an analysis on the basis of whether

* A unit vector **n** is defined by $|\mathbf{n}| = 1$.

certain common approximations are made. First, one must look for the degree of *self-consistency*, that is, the degree to which the fields, sources, and individual electrons mutually interact with one another. As an example, in systems operating at low currents, certain effects due to the space charge of the electrons can be neglected that might otherwise be significant in high-current devices. Second, one must determine if the approximation of *linearity* has been made. This is a perturbative approach in which functional variables are written as a large zero-order term, usually an equilibrium initial value plus a small time- and spatially-varying perturbation. Such analyses are adequate for determining the small-signal or early-time behavior of systems, but can fail for large-signal amplitudes. Third, one might see *multiple time-scale expansions*, in which time averaging is used to separate rapidly, but periodically, varying phenomena from the slow evolution of average system properties. Such analyses can fail when large-scale system features vary rapidly. Fourth, in numerical simulations, it is not uncommon to see reduced treatments of some sort, to limit the computing time and memory demand to manageable levels. Again, to give an example, in particle code simulations, many times the calculation is limited to one or two spatial dimensions, with variations in the remaining variables neglected.

4.3 Waveguides

Waveguides act as ducts for propagating microwave radiation and, under the proper circumstances in the presence of an electron beam, the interaction region within which microwaves are generated. They come in a wide variety of shapes and sizes, depending on the needs of the user. Let us first consider the case of waveguides with perfectly conducting walls, with no variation of the cross section along the axis and no electrons or dielectric within the waveguide (i.e., a vacuum waveguide). If we take the curl of Equation 4.1 and use Equations 4.2 and 4.3, we find that **B** obeys the wave equation within the waveguide when the source terms **j** and ρ vanish on the right-hand sides of Equations 4.1 and 4.4:

$$\nabla^2\mathbf{B} - \frac{1}{c^2}\frac{\partial^2\mathbf{B}}{\partial t^2} = 0 \tag{4.9}$$

Similarly, taking the curl of Equation 4.2 and using Equations 4.1 and 4.4, we find that **E** obeys the same equation:

$$\nabla^2\mathbf{E} - \frac{1}{c^2}\frac{\partial^2\mathbf{E}}{\partial t^2} = 0 \tag{4.10}$$

Note that both of these equations are linear in the fields, **B** and **E**, so that the solutions are valid for any magnitude of the field.

To proceed, let us consider the two independent classes of solutions:*

- *Transverse magnetic* modes (TM, or E-modes) with no axial component of **B** (i.e., $B_z = 0$)
- *Transverse electric* modes (TE, or H-modes) with $E_z = 0$

In the former case, we express the transverse field components in terms of E_z, while in the latter, we express the transverse field components in terms of B_z. Because we have assumed an axial symmetry for our waveguide, we can write both **B** and **E** in the form

$$\mathbf{E}(\mathbf{x},t) = \mathbf{E}(\mathbf{x}_\perp)\exp\left[i\left(k_z z - \omega t\right)\right] \tag{4.11}$$

where $\mathbf{x}_\perp$ is a vector in the plane perpendicular to the z axis. The simplicity of this relation depends on the fact that the shape of the cross section has no variation along the axis or in time. In Equation 4.11, the *wavenumber* k_z is related to the wavelength along the axis of the waveguide, λ_w (which is not, in general, equal to the free-space wavelength $\lambda = c/f$), by

$$k_z = \frac{2\pi}{\lambda_w} \tag{4.12}$$

and the radian frequency ω is related to the frequency f by

$$\omega = 2\pi f \tag{4.13}$$

Now, for TM modes, using Equation 4.10 and the form in Equation 4.11, E_z obeys

$$\nabla_\perp^2 E_z - k_z^2 E_z + \frac{\omega^2}{c^2}E_z = 0 \tag{4.14}$$

where $\nabla_\perp^2$ is the portion of the Laplacian operator that describes variations in the transverse plane of the waveguide. Similarly, for TE modes, using Equation 4.9, B_z obeys

* Another possible solution, the *transverse electromagnetic mode*, with no axial electric or magnetic field, is permitted in certain geometries, for example, a coaxial cylindrical waveguide or a parallel-plate configuration; however, it is not supported by a hollow cylindrical waveguide or a rectangular waveguide.

$$\nabla_\perp^2 B_z - k_z^2 B_z + \frac{\omega^2}{c^2} B_z = 0 \tag{4.15}$$

Both Equations 4.14 and 4.15 must be solved subject to the boundary conditions in Equations 4.5 and 4.6 for perfectly conducting walls, that the electric field components tangential to the wall and the magnetic field components perpendicular to the wall all vanish.

In general, for waveguides without axial variation in the cross section, we expect that we can separate the cross-sectional variation in the fields from that along the axis and in time, so that we can write

$$\nabla_\perp^2 E_z = -k_{\perp,TM}^2 E_z \tag{4.16}$$

$$\nabla_\perp^2 B_z = -k_{\perp,TE}^2 B_z \tag{4.17}$$

The eigenvalues on the right-hand side of these equations, $k_{\perp,TM}$ and $k_{\perp,TE}$, will depend on the cross-sectional shape of the waveguide; we will give examples shortly. Thus, we can rewrite Equations 4.14 and 4.15 in the form

$$\left(\frac{\omega^2}{c^2} - k_{\perp,TM}^2 - k_z^2\right) E_z = 0 \tag{4.18}$$

$$\left(\frac{\omega^2}{c^2} - k_{\perp,TE}^2 - k_z^2\right) B_z = 0 \tag{4.19}$$

Because **E** and **B** cannot vanish everywhere within the waveguide interior, the terms in parentheses in each of these equations must vanish, conditions we rewrite as:

$$\omega^2 = k_{\perp,TM}^2 c^2 + k_z^2 c^2 + \equiv \omega_{co}^2 + k_z^2 c^2 \tag{4.20}$$

$$\omega^2 = k_{\perp,TE}^2 c^2 + k_z^2 c^2 + \equiv \omega_{co}^2 + k_z^2 c^2 \tag{4.21}$$

where we have defined the *cutoff frequency* ω_{co} (without the subscripted TM or TE) as

$$\omega_{co} = k_{\perp,TM} c \quad \text{or} \quad k_{\perp,TE} c \tag{4.22}$$

We call ω_{co} the cutoff frequency because it is the minimum frequency at which a given mode can propagate along the waveguide; for lower frequencies, the mode is cut off. To see this, reorder the equation to see that $k_z^2 = (\omega^2 - \omega_{co}^2)/c^2$. Thus, if $\omega^2 < \omega_{co}^2$, $k_z^2 < 0$. Since there is no energy supplied to a passive waveguide (our beams come later), this means that k_z must be imaginary, and the waves decline exponentially from the point at which they are launched.

Equations 4.20 and 4.21 are examples of *dispersion relations*, the relationship between k_z and ω, or equivalently between λ_w and f, that must be obeyed within a device. Note here that only the eigenvalue $k_\perp$ — or the cutoff frequency ω_{co} — varies from one system to the next, depending only on the geometry of the waveguide. We will show that there are in fact an infinite number of cutoff frequencies within a waveguide, each corresponding to a *normal mode* of oscillation for the waveguide. These normal modes are the natural modes of electromagnetic oscillation in the waveguide, analogous to the waves on a string fixed at both ends, where higher-order modes correspond to shorter and shorter wavelengths along the string. They are distinguished by several properties. If we excite one of the normal modes, the oscillation in this mode will persist in time. If we drive the system with an impulse, then at long times after any initial transients have decayed the wave pattern within the system will be a linear sum, or *superposition*, of a set of normal modes (another consequence of the linearity of Maxwell's equations in the absence of charges and currents). Alternatively, this sum pattern of normal modes will be found at one end of a long system if we excite it at the other end with an impulse. In the following sections, we consider two of the most common types of waveguides, those with rectangular and circular cross sections.

4.3.1 Rectangular Waveguide Modes

Let us first consider a waveguide with rectangular cross section as shown in Figure 4.1, oriented so that a is the long dimension, $a \geq b$. The walls extend parallel to the x axis from x = 0 to x = a, and parallel to the y axis from y = 0 to y = b. In this geometry, $\mathbf{x}_\perp$ is a vector in the x-y plane, and the eigenvalue equations in Equations 4.16 and 4.17 become

$$\nabla_\perp^2 E_z = \left(\frac{\partial^2}{\partial x^2} + \frac{\partial^2}{\partial y^2}\right) E_z = -k_{\perp,TM}^2 E_z \tag{4.23}$$

$$\nabla_\perp^2 B_z = \left(\frac{\partial^2}{\partial x^2} + \frac{\partial^2}{\partial y^2}\right) B_z = -k_{\perp,TE}^2 B_z \tag{4.24}$$

The boundary conditions are the following:

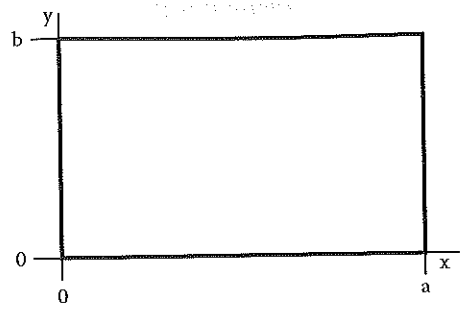

FIGURE 4.1
Cross section of a rectangular waveguide.

$$B_x(x=0,y)=B_x(x=a,y)=0\ ,\ 0\le y\le b \tag{4.25a}$$

$$B_y(x,y=0)=B_y(x,y=b)=0\ ,\ 0\le x\le a \tag{4.25b}$$

$$E_y(x=0,y)=E_z(x=0,y)=E_y(x=a,y)=E_z(x=a,y)=0\ ,\ 0\le y\le b \tag{4.25c}$$

$$E_x(x,y=0)=E_z(x,y=0)=E_y(x,y=b)=E_z(x,y=b)=0\ ,\ 0\le x\le a \tag{4.25d}$$

One can easily show that the solution to Equation 4.23 for the TM wave subject to the boundary conditions in Equation 4.25 is

$$E_Z=D\sin\left(\frac{n\pi}{a}x\right)\sin\left(\frac{p\pi}{b}y\right) \tag{4.26}$$

where D is a constant related to the amplitude of the wave. We can see from Equation 4.26 that for TM waves, neither n nor p can be zero. The eigenvalue and cutoff frequency are thus

$$k_{\perp,TM}(n,p)=\frac{\omega_{co}(n,p)}{c}=\left[\left(\frac{n\pi}{a}\right)^2+\left(\frac{p\pi}{b}\right)^2\right]^{1/2} \tag{4.27}$$

Similarly, one can show that the TE mode solutions are

$$B_z=A\cos\left(\frac{n\pi}{a}x\right)\cos\left(\frac{p\pi}{b}y\right) \tag{4.28}$$

TABLE 4.1

Expressions for the TM and TE Field Quantities for a Rectangular Waveguide in Terms of the Axial Field Component, Derived from Equations 4.1 to 4.4

Transverse Magnetic, $TM_{n,p}$	Transverse Electric, $TE_{n,p}$
$E_z=D\sin\left(\frac{n\pi}{a}x\right)\sin\left(\frac{p\pi}{b}y\right)$	$B_z=A\cos\left(\frac{n\pi}{a}x\right)\cos\left(\frac{p\pi}{b}y\right)$
$B_z=0$	$E_z=0$
$E_x=i\frac{k_z}{k_\perp^2}\frac{\partial E_z}{\partial x}$	$E_x=i\frac{\omega}{k_\perp^2}\frac{\partial B_z}{\partial y}$
$E_y=-i\frac{k_z}{k_\perp^2}\frac{\partial E_z}{\partial y}$	$E_y=-i\frac{\omega}{k_\perp^2}\frac{\partial B_z}{\partial x}$
$B_x=-i\frac{\omega}{\omega_{co}^2}\frac{\partial E_z}{\partial y}$	$B_x=i\frac{k_z}{k_\perp^2}\frac{\partial B_z}{\partial x}$
$B_y=i\frac{\omega}{\omega_{co}^2}\frac{\partial E_z}{\partial x}$	$B_y=i\frac{k_z}{k_\perp^2}\frac{\partial B_z}{\partial y}$
$\omega_{co}=k_\perp c=\left[\left(\frac{n\pi c}{a}\right)^2+\left(\frac{p\pi c}{b}\right)^2\right]^{1/2}$	

$$k_{\perp,TE}(n,p)=\frac{\omega_{co}(n,p)}{c}=\left[\left(\frac{n\pi}{a}\right)^2+\left(\frac{p\pi}{b}\right)^2\right]^{1/2} \tag{4.29}$$

In this case, either, but not both, n or p can vanish. Table 4.1 contains the mathematical expressions for the other field components in terms of the axial field component. We see that the eigenvalues for the TE and TM modes are exactly the same, a situation that we will see does *not* hold for the normal modes of a cylindrical waveguide.

Note that the cutoff wavelength for the mode with the lowest cutoff frequency, the TE_{10} mode (known as the *fundamental mode* for a rectangular waveguide), is twice the long dimension of the waveguide:

$$\lambda_{co}(1,0)=\frac{2\pi c}{\omega_{co}(1,0)}=2a$$

This feature has practical significance, based on a historical precedent. The standard designation for the many sizes of waveguide that are commonly built is the *WR number*, which stands for "waveguide, rectangular." The long

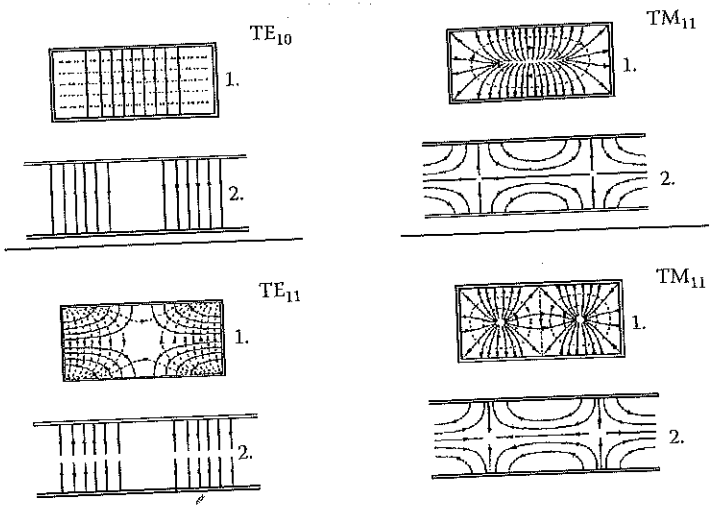

FIGURE 4.2
Field patterns for four of the lowest-order modes of a rectangular waveguide. In each case, the upper plot shows the fields in the cross section of the waveguide, the x-y plane, while the lower plot shows the fields in the y-z plane. (From Saad, T.S. et al., *Microwave Engineers Handbook*, Vol. 1, Artech House, Norwood, MA, 1971. With permission.)

dimension, commonly called a, measured *in inches*, is multiplied by 100 to give the number of the guide. So, a rectangular waveguide with a = 2.84 inches is called WR284. The guide has a cutoff in fundamental of 2.08 GHz and is optimal if operated in the 2.6- to 3.95-GHz band. A table of standard rectangular waveguide properties appears in the formulary (see Problem 1).

Field plots for four of the lowest-order modes in a rectangular waveguide are shown in Figure 4.2. Let us return to the dispersion relations in Equations 4.20 and 4.21. Dispersion relations are an essential tool in understanding waves in waveguides and cavities and how they interact with electrons to generate microwaves. We rewrite these equations in the form of an equation for ω (dropping the subscripts on $k_\perp$ for convenience):

$$\omega = \left(k_\perp^2 + k_z^2\right)^{1/2} c = \left(k_z^2 c^2 + \omega_{co}^2\right)^{1/2} \tag{4.30}$$

There is a different cutoff frequency for each mode, $TM_{n,p}$ or $TE_{n,p}$, so that there are, in fact, a hierarchy of such dispersion curves. Remember that we have oriented the waveguide so that a ≥ b, so that the lowest cutoff frequency is that for the $TE_{1,0}$ mode. To understand the physical significance of the cutoff frequency, note that if we establish the correspondence that $k_\perp^2 \sim k_x^2 + k_y^2$, with $k_x \sim n\pi/a$ and $k_y \sim p\pi/b$, then Equation 4.30 is essentially the dispersion relation for an electromagnetic wave propagating in free space, $\omega = kc = (k_x^2 + k_y^2 + k_z^2)^{1/2} c$. From a ray-optic viewpoint, we can view wave propagation within a rectangular waveguide as if a plane wave were reflecting from the walls with a wavefront perpendicular to the wavevector $\mathbf{k} = \hat{x}k_x + \hat{y}k_y + \hat{z}k_z$. Because the perpendicular component of **B** and the tangential component of **E** must vanish at the walls of this bounded geometry, the values of k_x and k_y are quantized. In Table 4.1, we see that n and p cannot both simultaneously vanish, or the field quantities would become infinite because $k_\perp$ would vanish.

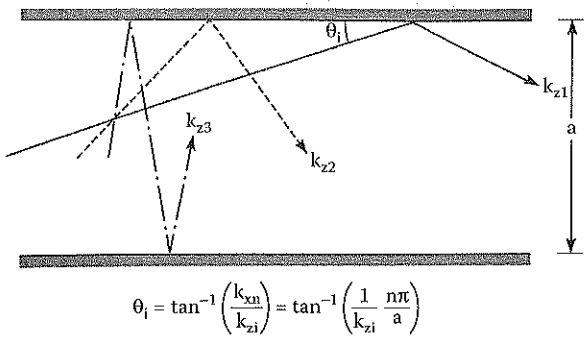

FIGURE 4.3
Ray diagrams for waves traveling along a rectangular waveguide. As i increases from 1 to 3, k_{zi} approaches 0 and the wave approaches cutoff.

In Figure 4.3, we see that as $k_z \to 0$, the direction of wave propagation along **k** becomes perpendicular to the axis, so that wave energy no longer propagates along the axis. Figure 4.4 is a plot of Equation 4.20 or Equation 4.21 for a single mode. For a given mode, we can see that there is no solution for ω in the range $0 \le \omega < \omega_{co}$, and there are no real values of ω for any mode below the lowest cutoff frequency for n = 1 and p = 0. On the other hand, for waves at a given frequency f, a waveguide can support every mode that has a cutoff frequency below ω = 2πf. For example, imagine that we excite a waveguide with dimensions 7.214 × 3.404 cm, the dimensions for the WR284 waveguide, at f = 5 GHz. The lowest cutoff frequencies for the TE and TM modes are shown in Table 4.2. We can see that as many as five modes could be excited by a 5-GHz signal — $TE_{1,0}$, $TE_{2,0}$, $TE_{0,1}$, $TE_{1,1}$, and $TM_{1,1}$ — the cutoff frequency for the last two being the same, since the TE and TM modes have the same cutoff frequencies in rectangular waveguides (although there are no $TM_{0,p}$ or $TM_{n,0}$ modes). The cutoff frequencies for higher-order modes lie above the 5-GHz signal, so they will not be excited.

As a last point in this discussion of rectangular waveguides, we introduce the two important velocities associated with wave propagation: the *phase velocity*, v_ϕ, which is the speed at which the phase fronts advance along the axis,

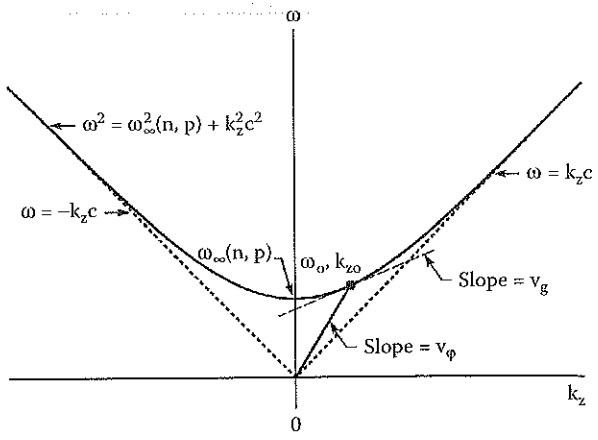

FIGURE 4.4
The dispersion relation between ω and k_z in Equation 4.30. The slopes of the two lines shown are defined in Equations 4.31 and 4.32.

TABLE 4.2

Cutoff Frequencies, Measured in GHz, for the Lowest-Order Modes of the WR284 Waveguide

n	p	$f_{co} = \omega_{co}/2\pi$ (GHz) a = 7.214 cm, b = 3.404 cm
1	0	2.079
0	1	4.407
1	1	4.873
1	2	9.055
2	0	4.159
2	1	6.059

$$v_\varphi = \frac{\omega}{k_z} \tag{4.31}$$

and the *group velocity*, v_g, which is the speed at which energy is transported along the axis,

$$v_g = \frac{\partial \omega}{\partial k_z} \tag{4.32}$$

In Figure 4.4, v_ϕ varies from ∞ at $k_z = 0$ to c for large values of the axial wavenumber, while v_g varies from 0 to c. The variation near $k_z = 0$ is consistent with our model of phase front motion in Figure 4.3; as the phase fronts becomes parallel to the walls of the guide, the phase velocity tends toward infinity, and as the waves bounce back and forth from one wall to the other, with no axially directed motion, the group velocity vanishes. For large values of k_z, the wavelength along the axis, $\lambda_w = 2\pi/k_z$, becomes much smaller than the cross-sectional dimensions of the guide, a and b, so that a mode propagates quasi-optically, with little effect from the waveguide.

4.3.2 Circular Waveguide Modes

Next consider a waveguide with circular cross section, with a perfectly conducting wall located at $r = r_0$. In this case, $\mathbf{x}_\perp$ lies in the r-θ plane. Further, we can write **B** and **E** in the form

$$\mathbf{E}(r,\theta,z,t) = \mathbf{E}(r,\theta)\exp\left[i(k_z z - \omega t)\right] \tag{4.33}$$

Now, Equations 4.16 and 4.17 take the forms

$$\nabla_\perp^2 E_z = \frac{1}{r}\frac{\partial}{\partial r}\left(r\frac{\partial E_z}{\partial r}\right) + \frac{1}{r^2}\frac{\partial^2 E_z}{\partial \theta^2} = -k_{\perp,TM}^2 E_z \tag{4.34}$$

$$\nabla_\perp^2 B_z = \frac{1}{r}\frac{\partial}{\partial r}\left(r\frac{\partial B_z}{\partial r}\right) + \frac{1}{r^2}\frac{\partial^2 B_z}{\partial \theta^2} = -k_{\perp,TE}^2 B_z \tag{4.35}$$

The boundary conditions in cylindrical geometry are the following:

$$B_r(r = r_0) = E_\theta(r = r_0) = E_z(r = r_0) = 0 \tag{4.36}$$

Expressions for the transverse field components in terms of the axial field components for both the TM and TE modes are given in Table 4.3. There, we also show the axial field solutions to Equations 4.34 and 4.35, subject to the boundary conditions of Equation 4.36. Note first that the solutions for the axial field terms involve Bessel functions of the first kind, J_p, several examples of which are plotted in Figure 4.5. These functions are oscillatory, although the period of oscillation in the radial direction is not fixed. Second, note that the eigenvalues for the TM and TE modes differ, unlike those for the rectangular waveguide, which are the same for both modes. As we show in the table, the eigenvalues for the TM modes involve the roots of J_p:

$$J_p(\mu_{pn}) = 0 \tag{4.37}$$

TABLE 4.3

Expressions for the TM and TE Field Quantities for a Circular Waveguide in Terms of the Axial Field Components, Derived from Equations 4.1 to 4.4

Transverse Magnetic, $TM_{p,n}$ ($B_z = 0$)	Transverse Electric, $TE_{p,n}$ ($E_z = 0$)
$E_z = DJ_p(k_\perp r)\sin(p\theta)$	$B_z = AJ_p(k_\perp r)\sin(p\theta)$
$E_r = i\frac{k_z}{k_\perp^2}\frac{\partial E_z}{\partial r}$	$E_r = i\frac{\omega}{k_\perp^2}\frac{1}{r}\frac{\partial B_z}{\partial \theta}$
$E_\theta = i\frac{k_z}{k_\perp^2}\frac{1}{r}\frac{\partial E_z}{\partial \theta}$	$E_\theta = -i\frac{\omega}{k_\perp^2}\frac{\partial B_z}{\partial r}$
$B_r = -i\frac{\omega}{\omega_{co}^2}\frac{1}{r}\frac{\partial E_z}{\partial \theta}$	$B_r = i\frac{k_z}{k_\perp^2}\frac{\partial B_z}{\partial r}$
$B_\theta = -i\frac{\omega}{\omega_{co}^2}\frac{\partial E_z}{\partial r}$	$B_\theta = i\frac{k_z}{k_\perp^2}\frac{1}{r}\frac{\partial B_z}{\partial \theta}$
$k_\perp = \frac{\omega_{co}}{c} = \frac{\mu_{pn}}{r_0}$	$k_\perp = \frac{\omega_{co}}{c} = \frac{\nu_{pn}}{r_0}$
$J_p(\mu_{pn}) = 0$	$J_p'(\nu_{pn}) = 0$

Note: A specific choice of sine functions has been made for convenience in the solutions for E_z and B_z, although both sines and cosines could be used. Note the ordering on the subscripts for the TE and TM modes; p and n are reversed, to be consistent with common practice.

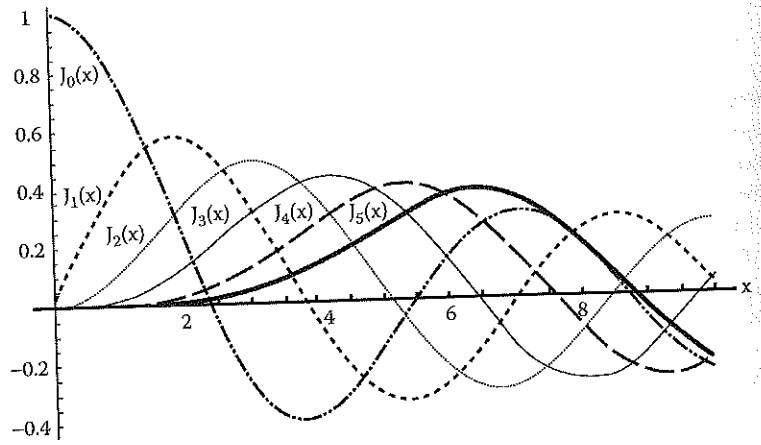

FIGURE 4.5
The first five Bessel functions of the first kind.

which for J_0 occur at x = 2.40, 5.52, 8.65, and so on. Similarly, the eigenvalues for the TE modes involve the roots of the derivatives of J_p:

$$\frac{dJ_p(x = \nu_{pn})}{dx} = 0 \tag{4.38}$$

In Figure 4.5, we can see, for example, that the derivative of J_0 vanishes at x = 3.83 (n = 1), 7.02 (n = 2), 10.2 (n = 3), and so on; the solution at x = 0 is not valid. Third, we note that we have made a choice with regard to the θ dependence of the solutions; both the sine and cosine are valid solutions for the axial field components of the TE and TM modes, and we have made specific choices in the absence of any wall perturbation that might disturb the symmetry in a perfectly cylindrical waveguide. Fourth, note that by historical convention, the TE and TM modes in circular waveguides have the indices ordered in a manner consistent with the ordering of indices on the roots of the Bessel functions in Equation 4.37 and the roots of the derivatives in Equation 4.38, so that for cylindrical modes we write TE_{pn} and TM_{pn}, with the azimuthal index first; *to emphasize, the first index is always the azimuthal index for cylindrical modes.*

In the rectangular waveguides, as the indices n and p vary, the spacing between eigenmodes depends on both dimensions, a and b. In circular waveguides, on the other hand, as n and p vary, there is only one dimensional parameter to consider, r_0, so that relative spacing between modes, after we normalize to the dimensional parameter c/r_0, is fixed. In Figure 4.6, we plot the normalized values of the cutoff frequencies for the lowest-order normal modes of a circular waveguide for positive values of p. The index n must be greater than 0, as we noted; however, the index p can range over positive and negative. In the absence of a beam, ω(p, n) = ω(−p, n); as we shall see later, though, this symmetry can be broken in the presence of a beam with rotating electrons. We see that the $TE_{1,1}$ mode has the lowest cutoff frequency of all modes in the circular waveguide. The figure also emphasizes the difference between the cutoff frequencies for the TE and TM modes. The dispersion relation for circular waveguides has exactly the same form as that shown in Figure 4.4, taking account of the difference in cutoff frequencies (see Problems 2 and 3).

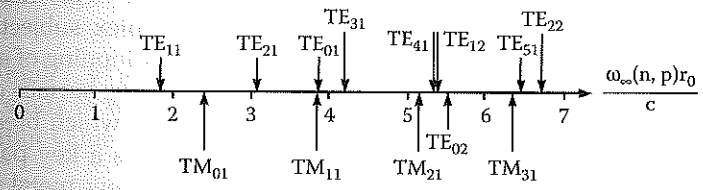

FIGURE 4.6
The cutoff frequencies for a circular waveguide, normalized to the factor c/r_0. The mathematical expressions for the cutoff frequencies are given in Table 4.3.